Three-Dimensional Self-Assembly of Rodcoil Copolymer Nanostructures

L. H. Radzilowski[†]

Materials Research Laboratory, Department of Materials Science and Engineering, Beckman Institute for Advanced Science and Technology, University of Illinois at Urbana—Champaign, Urbana, Illinois 61801

B. O. Carragher

Department of Cell and Structural Biology, Beckman Institute for Advanced Science and Technology, University of Illinois at Urbana—Champaign, Urbana, Illinois 61801

S. I. Stupp*

Materials Research Laboratory, Departments of Materials Science and Engineering and Chemistry, Beckman Institute for Advanced Science and Technology, University of Illinois at Urbana—Champaign, Urbana, Illinois 61801

Received July 3, 1996; Revised Manuscript Received January 27, 1997[⊗]

ABSTRACT: We have used electron tomography to characterize the self-assembly of nanostructures formed by rodcoil copolymers. The rodcoil copolymers used contained a perfectly monodisperse rod segment prepared by stepwise synthesis. The chemical compound rod segment is, in turn, covalently linked at one terminus to an end-functionalized polyisoprene segment prepared by living polymerization. We found that rodcoil molecules with rod volume fraction equal to 0.36 self-assemble into long strips with a nanoscale cross section. At lower rod volume fractions, the rodcoil molecules self-assemble into supramolecular aggregates with nanoscale *x*,*y*,*z* dimensions. Interestingly, the nanostructures organize into discrete layers of uniform thickness, containing in some cases a hexagonal 2D superlattice of rodcoil aggregates. Furthermore, nanostructures were found to self-assemble in all cases with three-dimensional order across the layers. The unique three-dimensional order observed in multilayers of the nanostructures must originate in the anisotropic aggregation of rod segments and the consequent space filling requirements as well as coil entropic penalties.

Introduction

Block copolymers consisting of rigid and flexible blocks expand the scope and complexity of microphase and nanophase separation phenomena. The highly disparate aspect ratios of rodlike and coillike component blocks are expected to affect greatly the details of molecular packing in condensed phases, and thus the nature of thermodynamically stable morphologies in these materials. Rodcoil block copolymers present interesting challenges to theoreticians and have, indeed, attracted a number of contributors in recent years.[1−8] There have been also an increasing number of synthetic efforts in this area within the last 10 years. A recent review[9] of block copolymer systems containing thermotropic liquid crystalline polymers describes two distinct classes of rodcoil structures, namely those having a coillike segment attached either to a side-chain liquid crystalline block[10−12] or to a main-chain liquid crystalline block.[13] Other experimental systems have utilized polypeptide blocks in α-helical conformation,[14−17] conjugated polymers,[18−22] or lyotropic mesogens[23] as the rigid segment in the main-chain architecture. We reported earlier on diblock rodcoil systems synthesized for the first time in our laboratory,[24] in which each macromolecule consists of a perfectly monodisperse, rigid rodlike segment covalently bonded to a flexible coillike segment of polyisoprene derived from living polymerization. These systems were the first ones and possibly the only ones so far which contain a perfectly monodisperse rod segment coupled with a truly flexible coil (a segment with subambient glass transition). The aperiodic rodlike segment of these rodcoil copolymers forms a compound that melts into a thermotropic liquid crystalline phase when not covalently attached to the coil.

We had previously observed that solution-cast thin films of our rodcoil diblock polymers nanophase separate into rod- and coil-rich domains that are less than 10 nm in dimension.[25] We have also observed that the morphologies depend sensitively on rod volume fraction.[25] Continuous striplike or slablike rod domains break up gradually into discrete aggregates with decreasing volume fraction of rod in the diblock polymer. This may be related in part to the high stretching free energies that coil blocks would experience if rodcoil polymers were assembled into continuous lamellae.[5] A similar effect was observed by Skoulios a long time ago in the ordered phases of soaps,[26] and more recently the stretching free energies for rodcoil polymers have been calculated by Raphaël and DeGennes[4] as well as Williams and Fredrickson.[5]

Since transmission electron microscopy (TEM) gives a two-dimensional (2D) projection of the material's structure, interpretation of the three-dimensional (3D) interdomain order can be ambiguous. One approach to overcome the problem would be to ultramicrotome cross sections that are perpendicular to the substrate plane. An alternative is electron tomography,[27−31] a technique that is especially useful in studying materials available in the small quantities generated by laboratory-scale syntheses. Literally meaning to visualize a slice, tomographic techniques produce a digital 3D image of an object that allows the viewing of its interior structure

---

[†] Current address: Department of Materials Science and Engineering, Massachusetts Institute of Technology, Cambridge, MA 02139.

[⊗] Abstract published in *Advance ACS Abstracts,* March 1, 1997.

S0024-9297(96)00970-9 CCC: $14.00

and are, therefore, widely used in medical imaging. Most applications of electron tomography have been limited to biological objects with high degrees of symmetry, such as crystals[32] and cylindrical filaments,[33] and more recently asymmetrical structures such as chromosomes[34] and the golgi apparatus.[35] There have been relatively fewer applications in materials science. One example is the work of Spontak et al., who studied the morphologies of block copolymers and block copolymer blends and were able to resolve cylindrical domains[36] and features of the ordered tricontinuous double-diamond[37] and double-gyroid morphologies.[38] In this article, we study the 3D self-assembly of nanostructures formed by rodcoil polymers through the use of electron microscopy and electron tomography. The study focuses on the effect of rod volume fraction in these self-assembling polymers.

Experimental Section

The materials studied in this work were first described in our earlier paper.[25] A series of rodcoil polymers were synthesized by attaching covalently functionalized polyisoprene chains (coil segments) with molecular weights of 3200, 4200, and 5400 to monodisperse rod segments, to give rod volume fractions (f_{rod}) of 0.36, 0.30, and 0.25, respectively. Coils were synthesized by living anionic polymerization and had polydispersities in the range of 1.04−1.08. Experimental samples were also prepared as before,[25] except that more concentrated solutions (0.1 wt %) were used in order to obtain thicker films. After annealing of the films at 140 °C for 12 h and staining with vapors of osmium tetraoxide, gold particles (10 nm diameter) were deposited on the sample surface by placing a drop of colloidal gold solution (Aldrich) on the specimen and blotting it dry. Concentration of the as-received solution was increased by centrifuging a small aliquot, pipetting off the supernatant, and redispersing the concentrated colloidal gold in an ultrasonic bath. The locations of these particles, fiducial markers, on the projected images were used during the image reconstruction process in electron tomography.

Projections were recorded with a Phillips CM-12 TEM at 100 kV using a single-axis tilt stage. To help minimize exposure to the electron beam and consequent shrinkage, samples were irradiated in the TEM for approximately 10 min prior to gathering projections. Most shrinkage occurs within the first minutes of exposure, and thus preirradiating reduces error introduced by simultaneous shrinkage and data collection. A projection was recorded at 0° tilt upon insertion of the sample into the microscope and then both immediately before and after data collection in order to measure the amount of in-plane sample shrinkage according to the positions of fiducial markers (ca. 1%). The TEM was operated in low-dose mode while recording projections, which limits exposure to the target area only to periods required for photographic recording. Images were recorded at 45 000× magnification at 2° increments of tilt angle, beginning at +60° and finishing at −60°, for a total of 61 images. An area having a sufficient number of fiducial markers (at least eight over an area of approximately 9×10^4 nm^2) was targeted and focused on after each tilt increment. Using the low-dose operation, this was done by focusing on an area adjacent and along the tilt axis, again to minimize beam exposure to the desired area.

The computational part of the reconstruction process was performed using a computer code developed at the San Diego Microscopy and Imaging Resource, University of California, San Diego. Raw data were input by digitizing the target area of each negative of the tilt series using a LeafScan 35 negative scanner with a spot size of 50 μm, to give a final image size of 512 × 512 pixels. A fiducial marker alignment program (Saxsalign) was used next in order to align all images with respect to a common tilt axis, made necessary by a noneucentric goniometer or a lack of consistent orientation while digitizing. Coordinates were first assigned to several gold particles common to each projection (at least eight) using the program Fido and a mouse-driven cursor to directly mark particles as they appeared on a graphics monitor. The coordinates were then passed to Saxsalign, which calculated a least-squares solution between the actual particle locations and those determined for an ideal microscope. Using the parameters from this solution, the program accordingly rotated and translated each projection until they coincided with a common tilt axis. Next, the electron density of the projections was normalized in order to compensate for the change in distance through the sample that the incident beam must travel as a function of tilt angle. The density of each projection was scaled proportionally to the change in thickness by a factor of 1/cos θ, where θ is the tilt angle. However, little difference in the quality of the reconstruction was evident with and without normalization. Finally, the actual reconstruction was done using the radius-weighted back-projection method described above. The resolution of the reconstructed image along the thickness direction was determined using eq 6 (see Appendix) with the following values: $T = 24 \pm 4$ nm, $N = 91$ (2° increments), $\gamma = \pm 58°$, and $A = 1.55$, thus giving a value of $d = 2.5 \pm 0.5$ nm. Noise was removed by low-pass filtering the reconstructed volume with a cutoff set equal to d, and slices were taken from the volume and examined using the software package Analyze. Comparisons of reconstructed volumes with model structures were also tried. These structures were prepared using the software suite of image processing tools known as Suprim. This package allowed us to build a digital 3D volume of a regular array of cylindrical or parallelepiped objects. The model volume was then imported into Analyze and examined in the same way as the reconstructed volumes.

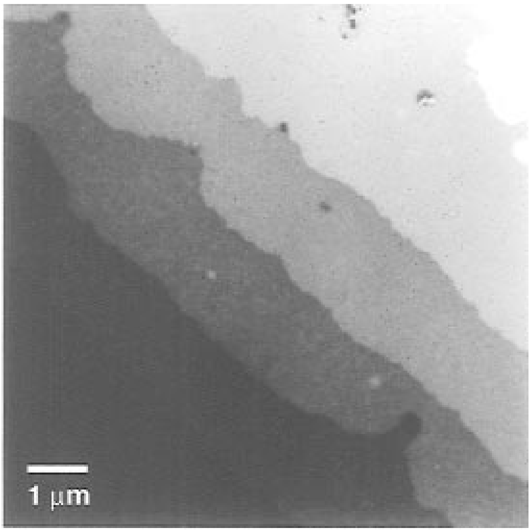

Figure 1. TEM micrograph of discrete steps (terraces) in a layered thin film of rodcoil copolymer, annealed at 140 °C for 12 h.

Results and Discussion

Upon annealing, solution-cast rodcoil films were observed to develop terraces, or discrete steps in film thickness (see Figure 1). The nanoscale morphologies observed on the first step correspond to those reported earlier[25] in films of thicknesses estimated to be 5−10 nm. TEM images of thicker regions reveal more complex, yet regular, morphologies, indicating highly ordered three-dimensional arrangements of rod domains through the film thickness direction.

Images were obtained from multistep regions for rodcoil polymers with the various rod volume fractions. As we reported earlier, the largest rod volume fraction ($f_{\text{rod}} = 0.36$) had a morphology of alternating rod- and coil-rich strips in a single step.[25] The rod strips measure 6−7 nm in width, approximately the extended molecular length of the rod segment. Interestingly, this morphol-

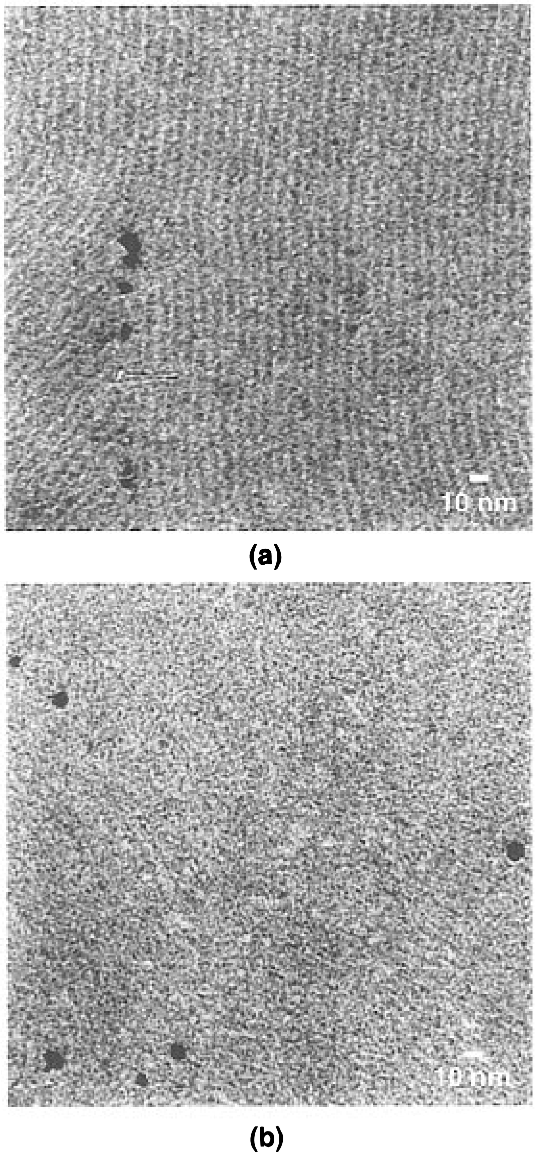

Figure 2. TEM micrographs of rodcoil copolymer with f_{rod} = 0.36, showing that an odd number of stacked layers generates the contrast of an alternating "strip" morphology of rod and coil domains (a), while an even number has virtually no contrast (b).

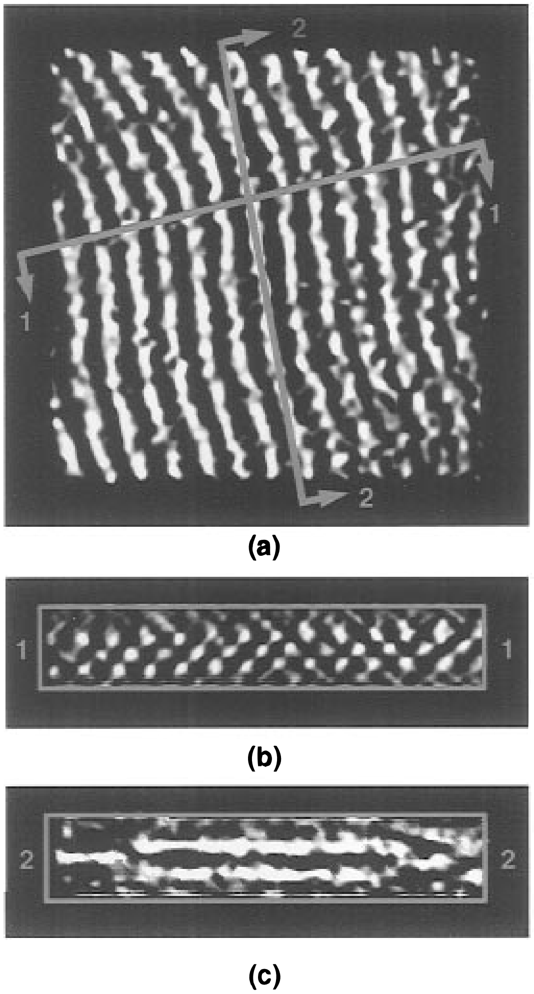

Figure 3. Slices from a reconstructed volume of rodcoil copolymer, f_{rod} = 0.36. (a) A slice parallel to the layer plane shows the characteristic strip morphology. Panels b and c show cross-sectional slices orthogonal to the layer plane and parallel to the corresponding section lines in (a). Panel b shows a checkerboard morphology.

ogy is observed in regions containing odd numbers of steps (Figure 2a) but is not observed in regions with even numbers of steps (Figure 2b). Contrast at even numbers of steps virtually disappears, giving no indication that nanophase separation of rod and coil segments has occurred. However, slices from reconstructed volumes reveal nanophase separation and even order in the 3D packing of rod domains. Figure 3a shows a slice parallel to the film plane, revealing the characteristic striplike morphology, while Figure 3b,c show slices that are orthogonal to the plane of the film, one perpendicular and one parallel to the strips, respectively. The slice taken perpendicular to the strips' long axis (Figure 3b) shows that the rod domains are not lamellae but discrete channel-like long objects, 6−7 nm in diameter. This figure also shows that the strips lie in layers, parallel to the surface. Each layer is displaced relative to those above and below such that coils surround each rod domain. The strip's long axis also remains parallel to the plane of the film, as indicated by the alternating layers of rod and coil domains shown in Figure 3c. This accounts for the odd−even contrast effect seen in TEM. Films with even numbers of layers have effectively uniform electron density across the sample plane and hence reveal minimum contrast. On the other hand, films with an odd number of layers will reveal contrast because the number of stacked rod domains will alternate across the sample plane (varying by one between adjacent stacks). The number of strip-containing layers (4) corresponds to the number of terraced steps at which projections were recorded for the reconstruction.

At the smallest volume fraction of rod segments (f_{rod} = 0.25), we observe a hexagonal superlattice of supramolecular aggregates, 6−7 nm in diameter (Figure 4a).[25] Based on the observed contrast, the aggregates contain the rod segments of rodcoil molecules, and the covalently attached coils splay to form the interaggregate matrix of the superlattice. Projections through multiple layers show an apparently continuous network of rod domains with good long-range order (Figure 4b). The power spectrum of this image (left inset), obtained from the fast Fourier transform of the digitized image, shows two orders of reflections having hexagonal order. A filtered image derived from the FFT (right inset) shows more clearly the regular arrangement of rod domains. Slices from the reconstructed volume taken in cross section (Figure 5) show that the self-assembled rod aggregates are discrete objects with approximately equal thickness and $x-y$ dimensions and, interestingly,

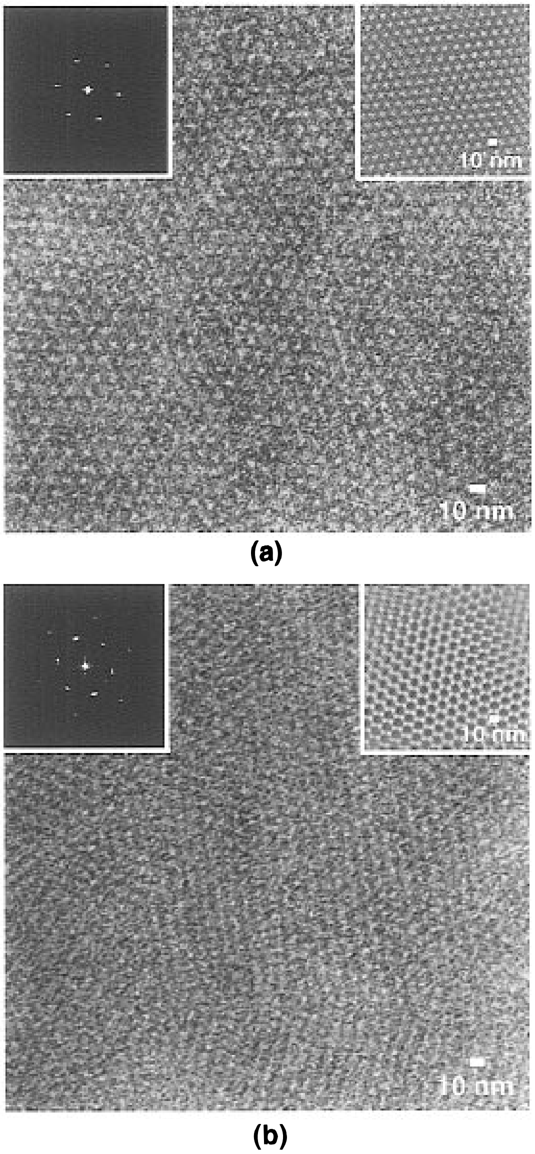

Figure 4. Morphologies observed for one layer (a) and for two or more stacked layers (b) in rodcoil copolymer with $f_{\mathrm{rod}} = 0.25$.

are ordered in layers parallel to the surface. Three-dimensional stacking order is maintained through the thickness direction, and the arrangement of aggregates, as expected, appears different depending on the slicing plane through the analyzed volume.

At intermediate rod volume fraction ($f_{\mathrm{rod}} = 0.30$), the morphology was shown to consist of both aggregate and strip domains in a single layer (Figure 6a).[25] Films composed of two or three stacked layers show a coexistence of the morphologies of Figures 2b and 4b. For films having more than three layers, however, we observe what appears to be hexagonally shaped cells fused at their sides to form a network pattern, with each cell containing a single rod aggregate in its center (Figure 6b). Compared to rod regions forming the apparent honeycomb wall, the center rod aggregate has stronger contrast relative to coil domains. A cross-sectional slice taken through some of the central aggregates of each honeycomb cell (Figure 7) reveals a combination of discrete aggregates of the same size as in the $f_{\mathrm{rod}} = 0.25$ system and "columns" of rod segments that span the film thickness. Also, there appears to be order between aggregates through the thickness. Figure 8 shows a series of slices from the reconstructed volume of $f_{\mathrm{rod}} = 0.30$ taken parallel to the layer plane at sequentially greater distances from the air−polymer interface. Each slice contains a 2D hexagonal superlattice of rod aggregates and is rotated with respect to the slices above and below by approximately 30° about an axis normal to the layer plane.

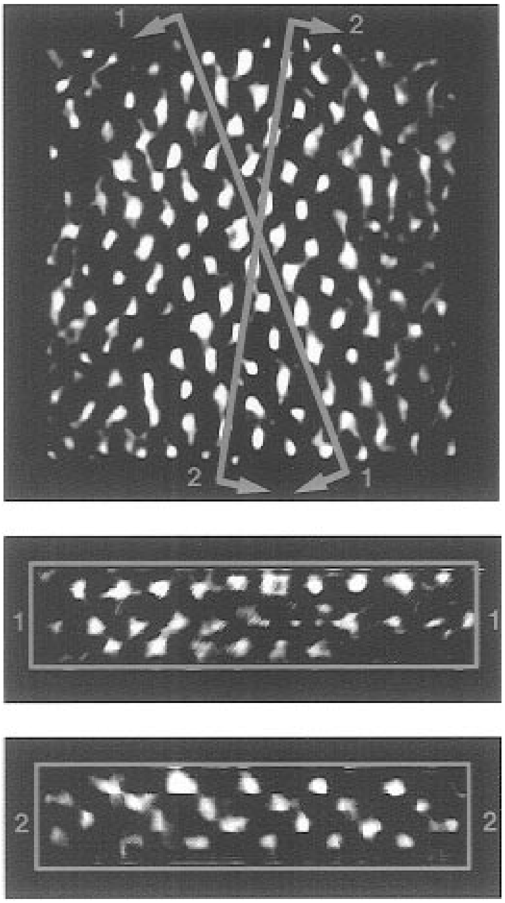

Figure 5. Slices from a reconstructed volume of rodcoil copolymer, $f_{\mathrm{rod}} = 0.25$, at different orientations with respect to the superlattice.

From the slices of the reconstructed volumes, we see that self-assembled rod domains order into 2D layers parallel to the substrate surface. Each terraced step contains an integral number of layers stacked with specific registration. The formation of terraces is well known in thin films of coil−coil block copolymers containing lamellae[39−41] and cylinders.[42] One work in particular has looked at the ordering of spheres and cylinders and observed similarly layered morphologies.[43] An interesting aspect of the rod−coil polymers studied here is the dependence of stacking order on volume fraction of rod segments.

In the strip morphology ($f_{\mathrm{rod}} = 0.36$), the schematic of Figure 9 illustrates that layers are correlated such that each strip resides over a coil region of the adjacent layer and that the direction of its long axis remains constant through the layers. Interestingly, the direction of strips through the thickness of the film is maintained as rod domains meander in the plane of the film. This order is reminiscent of the hexagonal packing of cylinder domains of coil−coil block copolymers. In general, the order in which block copolymer domains assemble reflects the need to minimize the amount of stretching that coils must sustain in order to fill space and maintain a uniform segmental density.[44−46] In the case of cylinders, a hexagonal packing with long axes aligned has the lowest coil stretching energy of any other

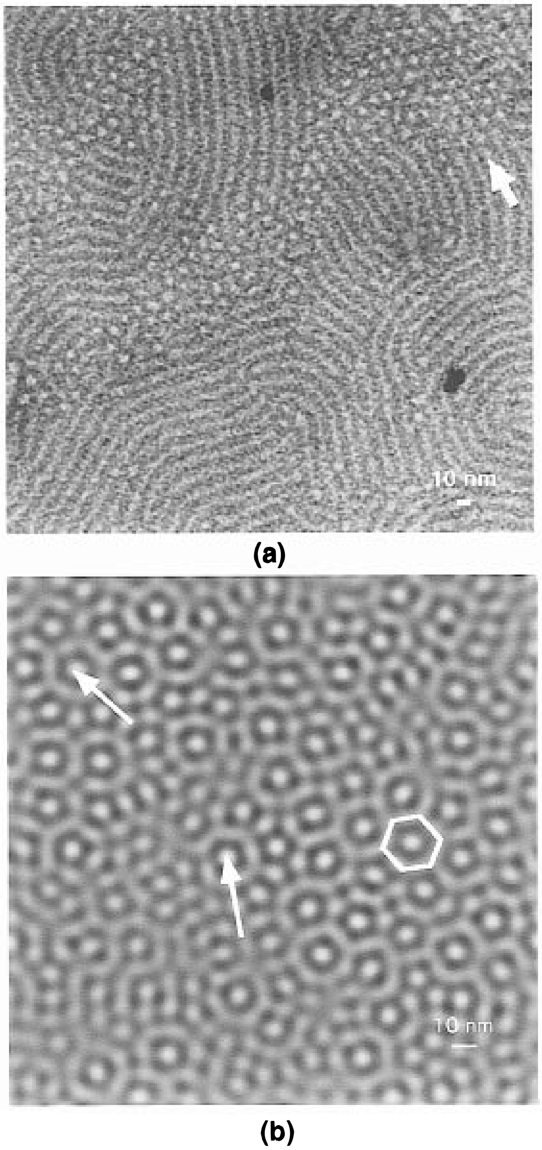

Figure 6. Morphology of rodcoil copolymer, $f_{\mathrm{rod}} = 0.30$, observed for one layer (a) and for three or more stacked layers (b). Arrows in (b) point to evidence of rotation in the stacked layers.

arrangement.[47] Even though the strip morphology is somewhat analogous to the cylindrical phase of block copolymers, it is clear that some key differences exist which must be linked to the rodcoil as opposed to coil–coil architecture of the molecules. For example, while the reconstruction performed here lacks the resolution necessary to discern the exact cross-sectional shape of strip domains, slices from the reconstructed volume reveal the strips' cross section dimension to be 6–7 nm, and this cross section is too small to be interpreted as the radial arrangement of rodcoil molecules. In flexible copolymers, on the other hand, a radial trajectory of molecules within cylindrical volumes is a key feature of the phase. Instead, rods within the strips must be assembled into interdigitated bilayers or monolayers in order to be consistent with the observed dimensions. A dimension of 6–7 nm corresponds roughly to the extended length of rod segments. Thus, interdigitation of rods would be an appropriate model. This model would be, in fact, more favorable than assembly into monolayers for two reasons. One is enthalpic in nature, because interdigitated bilayers reduce unfavorable contacts between rods and coils. A second reason, of entropic character, is the greater volume created for coils to explore conformational space in the lower "grafting density" of an interdigitated bilayer. If rods were assembled as perfect monolayers or interdigitated bilayers, one could invision the strips as having the square cross section shown in Figure 9. However, the rodcoil junctions may not be highly localized to a planar surface dividing rod and coil segments; the surface may instead by roughened, producing long objects with irregular cross sections. An open question still remaining is the orientation of rod segments within the strip domains. This issue will be dealt with in a subsequent publication.

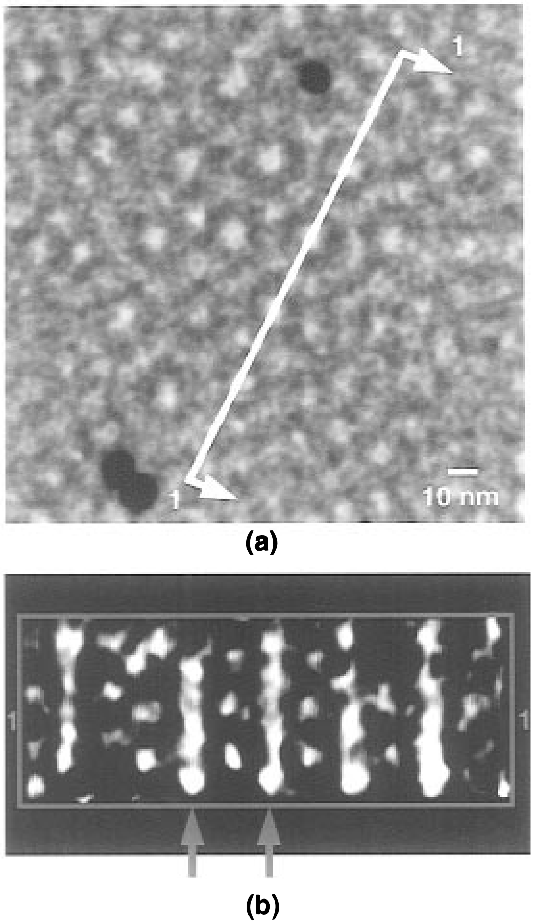

Figure 7. Cross-sectional slice from a reconstructed volume of rodcoil copolymer, $f_{\mathrm{rod}} = 0.30$. The slice in (b) was taken through a series of central "core" aggregates shown in the 0° tilt projection (a). In the slice, the cores can be seen to span the film's thickness.

The effect of f_{rod} on stacking order is most apparent for the aggregate rod domains. Examination of the slices taken from the reconstructed volume of $f_{\mathrm{rod}} = 0.25$ shows that each layer contains a hexagonal superlattice and that they stack with the same registration that close-packed planes of atoms do. This is verified by comparing actual slices with ones taken from a model structure having the proposed 3D packing of rod domains. Figure 10 makes this comparison for slices taken at the same relative orientation and shows good agreement. This stacking arrangement positions a rod domain above an interstitial site on an adjacent superlattice, as shown in the schematic of Figure 11. When the rod volume fraction is increased to $f_{\mathrm{rod}} = 0.30$, the layers maintain the hexagonal arrangement of aggregates but are stacked very differently. The most prevalent morphology at $f_{\mathrm{rod}} = 0.30$ appears as a

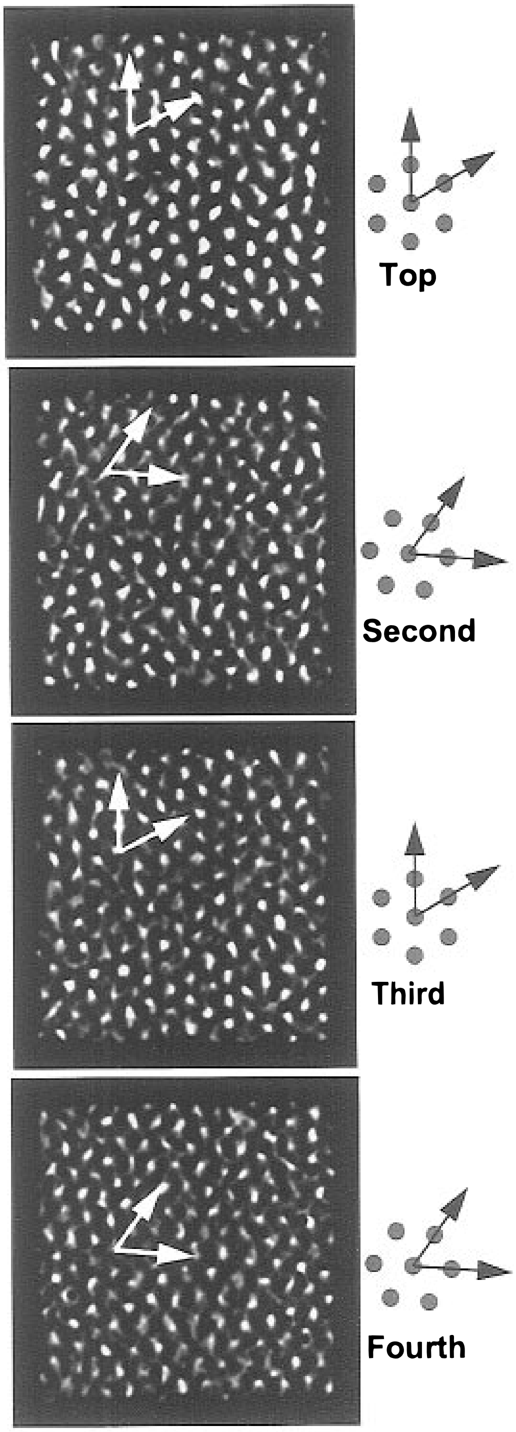

Figure 8. Slices from a reconstructed volume of rodcoil copolymer, $f_{\mathrm{rod}} = 0.30$, parallel to the layer plane. The slices were taken at adjacent layers, each one revealing a hexagonal superlattice of rod aggregates. Superlattices in adjacent layers alternate in orientation by 30°.

honeycomb in projection, as shown in Figure 12a. An FFT of the selected area in Figure 12a shows a set of 12 first-order reflections (Figure 12b). Higher order reflections are not observed. In Figure 12c, a 2D hexagonal reciprocal lattice ($a^* = b^*$; $\gamma = 59°$) with a lattice parameter of 13.3 nm would generate one-half of the (10)-type reflections. A similar reciprocal lattice rotated 30° relative to the first explains the remaining reflections, but the lattice parameter must be 12.3 nm. The honeycomb pattern shown clearly in the Fourier-filtered, selected area of Figure 12a (Figure 12d) may be explained by an alternating pattern of expanded and contracted 2D superlattices, as is demonstrated by the schematic projection in Figure 13, which was produced by a superposition of two rotated superlattices with different lattice parameters. Places where the continuity of the honeycomb pattern is disrupted may be caused by defects and grain boundaries in individual layers. An uncommon morphology observed in some areas of these films is rotated superlattices, apparently without the alternating expansion of lattice parameter (see Figures 6b and 14). This morphology produces a 2D projection similar to that shown in the model of Figure 15. The arrows in Figure 6b point to aggregates that may be thought of as the centers about which rotation of layers occurs. From these centers radiate the "spokes" that are characteristic of Figure 15. A similar rotation pattern has been observed in thin films of a polystyrene−polybutadiene diblock copolymer claimed to contain polybutadiene cylinders oriented normal to the substrate surface.[48] A possible explanation for the honeycomb stacking arrangement may be the structural diversity of the coil segments. Unlike the rod segments, which are a chemical compound, the polyisoprene coils are dissimilar owing to the different modes of isoprene addition (1,4 vs 1,2 vs 3,4), cis−trans isomerism, and the Poisson molecular weight distribution. Superlattices of alternating lattice constants may be one way of accommodating different populations of rodcoils having structurally diverse coils.

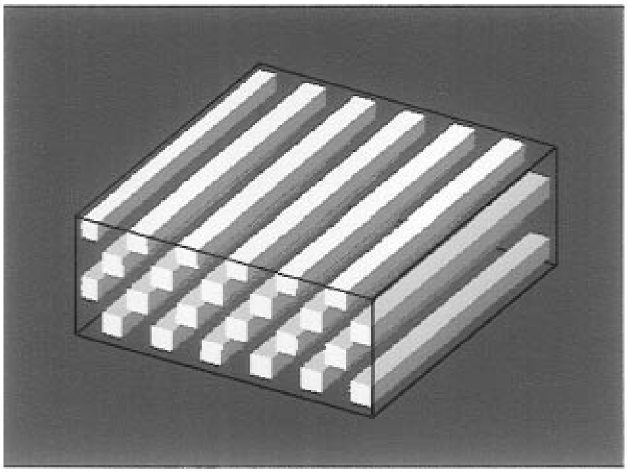

Figure 9. Schematic of the stacking arrangement of "strip" rod domains with a checkerboard cross section.

The 3D morphologies of the self-assembled nanostructures formed by these rodcoil molecules ($f_{\mathrm{rod}} = 0.25$ and 0.30) exhibit differences with respect to those of coil−coil block copolymers. Spherical domains of coil−coil copolymers, for example, are observed to order into a hexagonal superlattice for films of approximately monolayer thickness but form a BCC superlattice in the bulk.[49] However, the close-packed morphology of $f_{\mathrm{rod}} = 0.25$ is maintained over as many as seven layers and is probably very similar to the bulk state. At the increased rod volume fraction of 0.30, 2D superlattices of the self-assembled nanostructures order in a significantly different way. This is in contrast to coil−coil copolymers, which typically show the same equilibrium lattice type over the compositional window in which a given morphology is stable. The BCC superlattice, for example, is preferred at all volume fractions in which spherical domains form in the bulk. A consideration in comparing the behavior of rodcoil vs coil−coil copolymers is the interface between rod and coil junctions. We suggest that rodlike segments within the nanostructures are

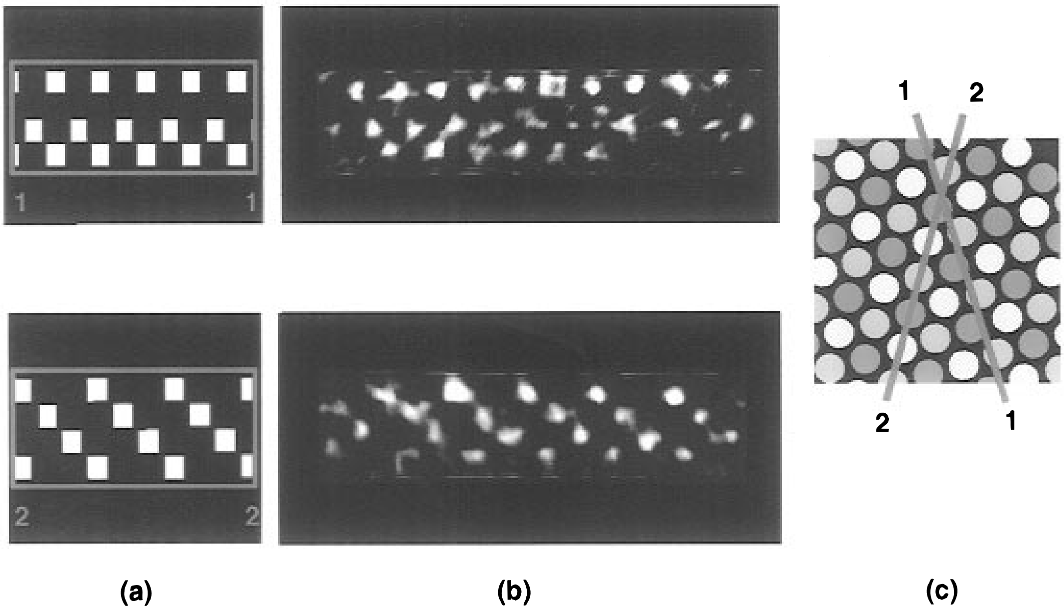

Figure 10. Comparison of slices from simulated (a) and reconstructed volumes of rodcoil copolymer, $f_{\mathrm{rod}} = 0.25$ (b). A schematic projection (c) of the proposed stacking order shows the relative orientations of the respective slices.

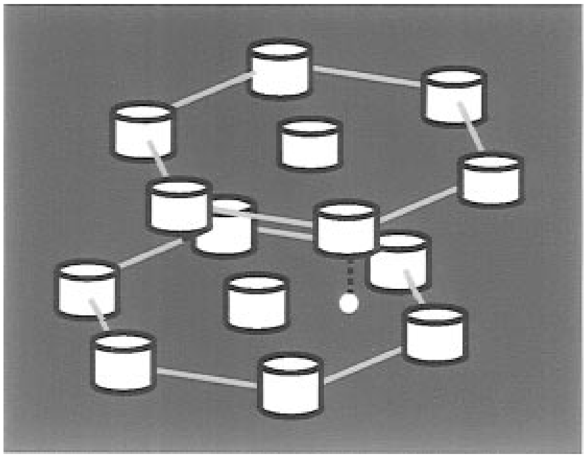

Figure 11. Schematic of close-packed stacking of hexagonal superlattices.

orientationally ordered, and thus one does not expect a uniform density of coil segments surrounding the rod clusters. In coil−coil micelles, on the other hand, coils radiate over the entire surface. The ordering of spherical micelles is thought to depend on the extent to which neighboring coronal coils overlap and interpenetrate with those of other micelles in order to fill space with a uniform segmental density.[44,49,50] In this context, rod domains with nonuniform coil densities may pack with their neighbors in unique ways in order to fill space efficiently and maximize the entropy of the grafted coils.

Conclusions

The rodcoil copolymers studied here were found to self-assemble into layered nanostructures that form 2D superlattices and possess ordered 3D morphologies. Electron tomography revealed long strips with nanoscale cross section or nanometer-sized supramolecular aggregates in x,y,z dimensions organized into discrete layers. The nature of 3D order in the stacked nanostructures was found to depend on rod volume fraction. The unique 3D morphologies observed evidently originate in the anisotropic aggregation of rod segments and the consequent space filling requirements and coil entropic penalties.

Acknowledgment. This work was supported by National Science Foundation Grant DMR 89-20538, obtained through the Materials Research Laboratory of the University of Illinois. The electron microscopy work was performed in the Center for Microanalysis of Materials, University of Illinois, which is supported by the U.S. Department of Energy under Contract DEFG02-91-ER45439. Reconstructions were computed at the Beckman Institute Visualization Laboratory. John L. Wu of our laboratory synthesized the polymers, and L.H.R. gratefully acknowledges Eastman Kodak for a graduate fellowship.

Appendix: Principles of Tomographic Reconstruction

The input for a reconstruction is a series of 2D projections of a sample generated by a transmission electron microscope. The sample is held in the microscope's goniometer and tilted about either one (single axis tilting) or two orthogonal axes (conical tilting) while recording projections at equal angular increments over as wide a range as possible.[51] Various algorithms have been developed to compute the reconstructions, and several[52] are based on the relationship between an object and its projections in Fourier space, the Fourier transform being an essential element. A theorem key to the process states that the Fourier transform of an object's projection is a central plane in the Fourier transform of the object.[30] Figure 16 schematically shows this for the case of a 2D object, represented by the function $f(x,y)$, and single-axis tilt. In electron tomography, a projection is produced by parallel illumination from the electron source passing through the object tilted at an angle θ about an axis orthogonal to the beam path. The function $P_\theta(t)$ at a given θ represents the projection in real space. It is obtained using the Radon transform[30] by performing ray integrals of $f(x,y)$ along lines parallel to the electron beam for all points on the t axis, where t is related by

$$t = x \cos \theta + y \sin \theta \tag{1}$$

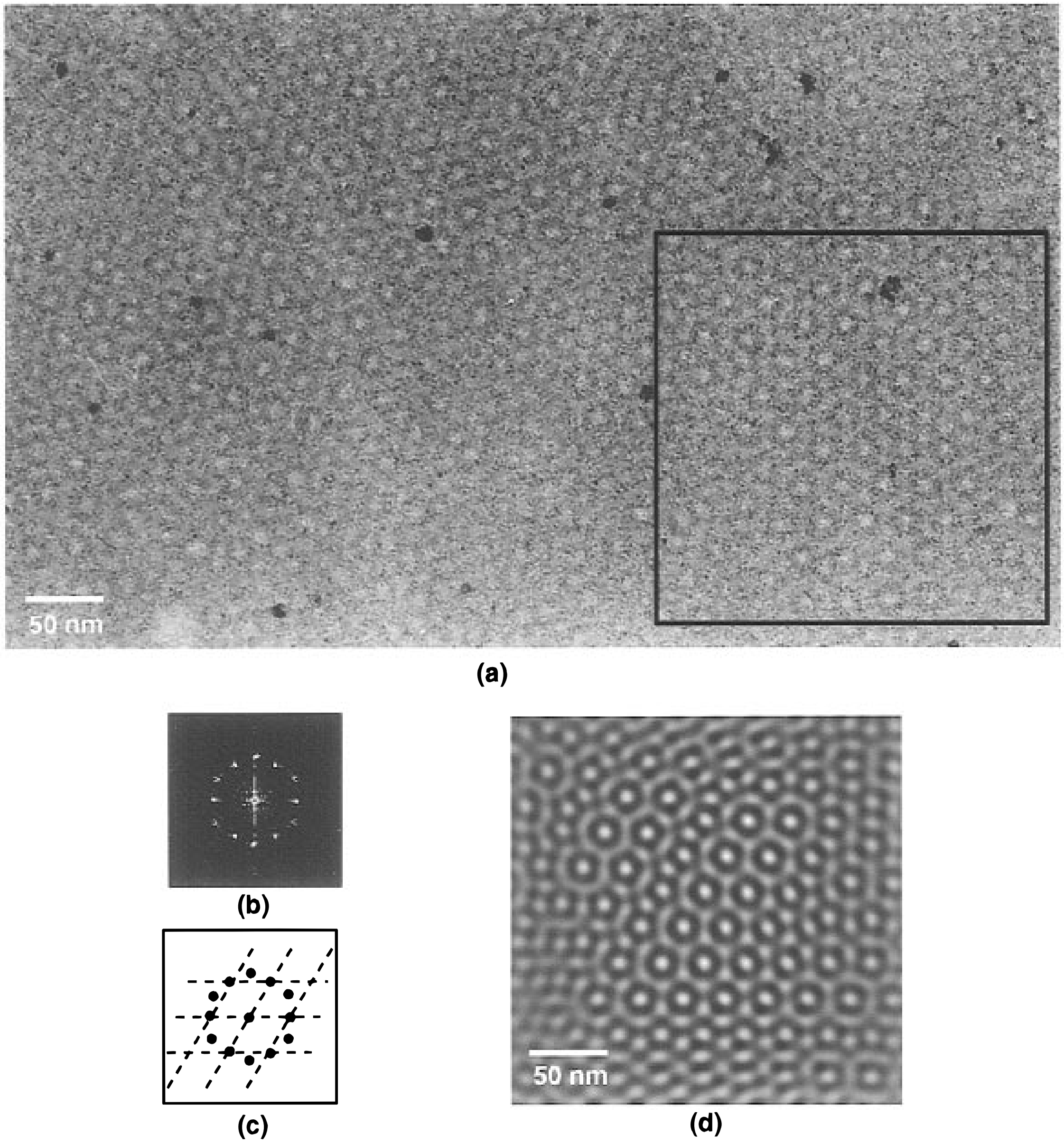

Figure 12. (a) TEM micrograph of a multilayered region of rodcoil copolymer, $f_{\mathrm{rod}} = 0.30$, showing a projection that resembles a honeycomb. (b) Power spectrum of the selected area in (a) showing first-order reflections of the (10) type. (c) Hexagonal reciprocal lattice constructed to fit one-half of the reflections, having a lattice parameter of 13.3 nm. A similar reciprocal lattice may be constructed for the other reflections, rotated 30° and with a lattice parameter of 12.3 nm. (d) Spot-pass filtered image of the selected area in (a).

By the central section theorem, the Fourier transform of $P_\theta(t)$ in polar coordinates is

$$J(w,\theta) = \int_{-\infty}^{\infty} P_\theta(t) \exp[-2\pi i w t]\, \mathrm{d}t \qquad (2)$$

where w is the spatial frequency. The Fourier coefficients, $J(w,\theta)$, are arranged along a line in Fourier space with the same angular orientation θ as the projection. When gathered over a range of tilt angles, these coefficients can be thought of as a sampling of a 3D Fourier transform of the object. Taking the inverse Fourier transform of the entire array of coefficients then gives the reconstructed volume in real space. As Figure 16 shows, the coefficients are arranged on a radial grid which, in practice, must be interpolated onto a square grid in order to perform an inverse transform. It is possible to interpolate between coordinate systems, but an alternative and more commonly used algorithm is the radius-weighted back-projection technique, in which the object is reconstructed in real space through back-projection and accompanied by a weighting process that uses the Fourier space relationship.[30,52] Back-projection works by first projecting values of $P_\theta(t)$ for a given θ back onto the $x-y$ plane of the object (Figure 16). At a given point on the t axis, the back-projected value of P_θ is the same everywhere in the $x-y$ plane along a line parallel to the electron beam. The reconstructed image density at any point in the $x-y$ plane, then, is the sum of all back-projections at that point,

$$\hat{f}(x,y) = \int_0^{\pi} P_\theta(x \cos \theta + y \sin \theta)\, \mathrm{d}\theta \qquad (3)$$

Distortion that is introduced by this algorithm may be removed by "weighting" the individual projections,

$$P_{\mathrm{w},\theta}(t) = \int_{-\infty}^{\infty} J(w,\theta)|w| \exp[2\pi i w t]\, \mathrm{d}w \qquad (4)$$

and then back-projecting according to eq 3. The spatial

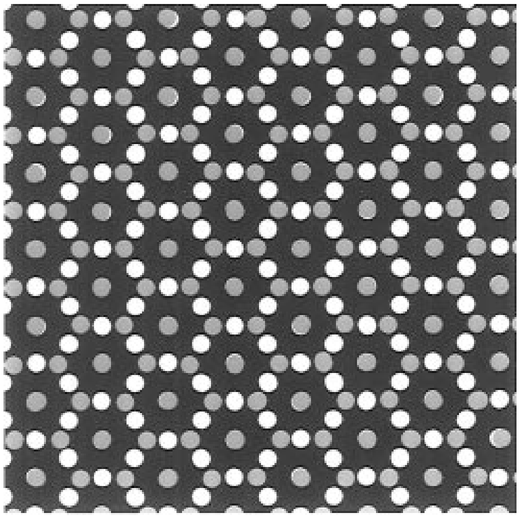

Figure 13. Model projection of two stacked hexagonal superlattices rotated 30° relative to each other and one uniformly expanded with respect to the other.

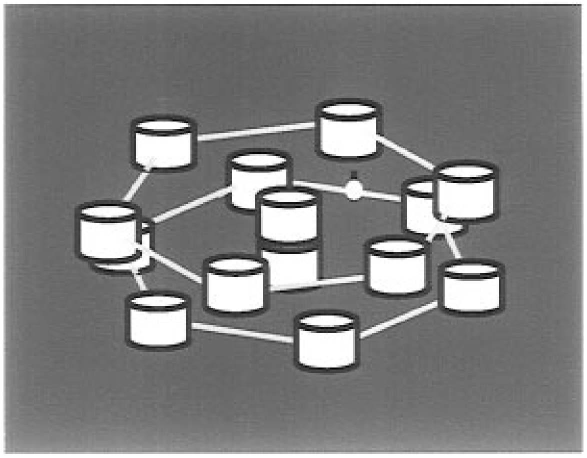

Figure 14. Schematic of stacked and rotated hexagonal superlattices.

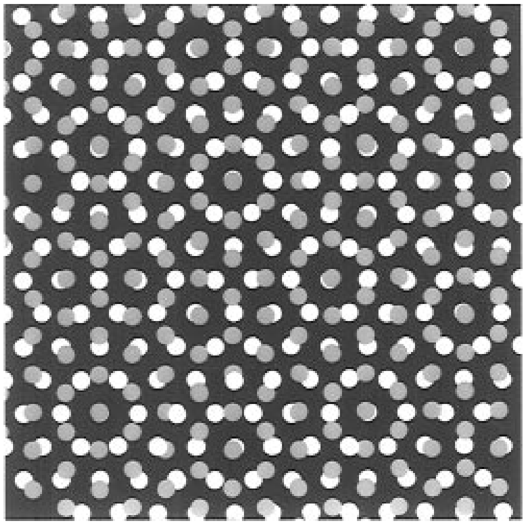

Figure 15. Model projection of two stacked hexagonal superlattices rotated 30° with respect to each other.

frequency term, w, in eq 4 is directly proportional to distance measured perpendicular to the tilt axis in Fourier space, and hence the term "radius-weighted" is given. Because of the relationship between an object and its projections in Fourier space, as described earlier, this weighting process is equivalent to deconvoluting the back-projected object by the point spread function of the back-projection algorithm.[51]

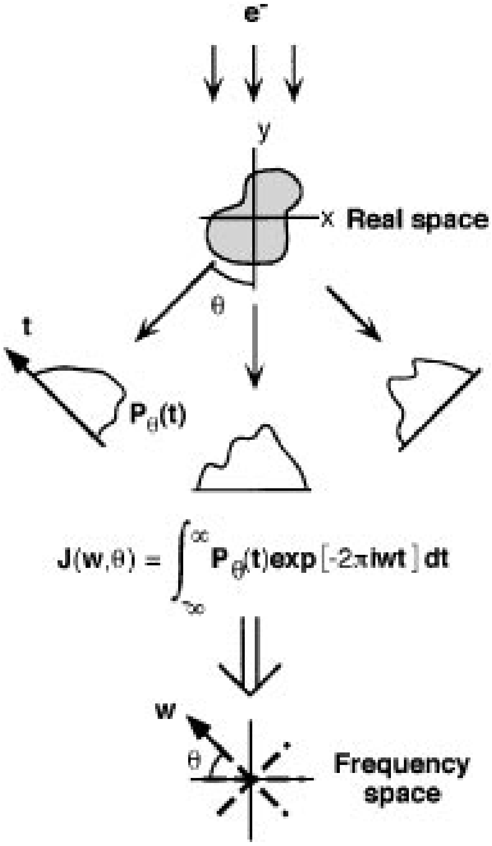

Figure 16. Schematic illustration of electron tomography and the central section theorem for a 2D object.

Reconstruction in practice requires facing certain limitations. For one, the physical arrangement of the electron gun and sample goniometer in a typical TEM does not allow the ideal 180° range of tilt needed to give a complete sampling of Fourier space. For the single-axis tilt arrangement, the missing information is a wedge-shaped region of Fourier space, resulting in a loss of resolution for the reconstructed volume in the direction parallel to the electron beam. An additional problem is that only a finite number of projections can be generated. Given the radial arrangement of the Fourier coefficients (Figure 16), more information will be missing with increasing spatial frequency. This effectively limits the reconstruction's resolution but may be compensated by increasing the number of projections gathered, since resolution is expressed as[53]

$$d = \pi D/N \tag{5}$$

where d is the size of the smallest feature that can be visualized in the reconstruction, D is the diameter (size) of the object or feature being reconstructed, and N is the number of projections. An expression that further takes into account the missing volume of Fourier space described above is[54]

$$d = \frac{\pi A T}{N \cos \gamma} \tag{6}$$

where T is the specimen thickness, N is the "ideal" number of projections that would be gathered over a 180° tilt range with a given increment, γ is the maximum tilt angle used, and A is a constant that approximates the resolution loss due to the restricted tilt range. Structural detail that is smaller than the minimum resolvable is considered noise and removed by low-pass filtering the reconstructed object to the limiting resolution.

References and Notes

(1) Semenov, A. N.; Vasilenko, S. V. *Sov. Phys. JETP* **1986**, *63*, 70.
(2) Halperin, A. *Macromolecules* **1990**, *23*, 2724.
(3) Semenov, A. N. *Mol. Cryst. Liq. Cryst.* **1991**, *209*, 191.
(4) Raphaël, E.; DeGennes, P. G. *Makromol. Chem. Macromol. Symp.* **1992**, *62*, 1.
(5) Williams, D. R. M.; Fredrickson, G. H. *Macromolecules* **1992**, *25*, 3561.
(6) Holyst, R.; Schick, M. *J. Chem. Phys.* **1992**, *96*, 730.
(7) Williams, D. R. M.; Halperin, A. *Phys. Rev. Lett.* **1993**, *71*, 1557.
(8) Singh, C.; Goulian, M.; Liu, A. J.; Fredrickson, G. H. *Macromolecules* **1994**, *27*, 2974.
(9) Chiellini, E.; Galli, G.; Angeloni, A. S.; Laus, M. *Trends Polym. Sci.* **1994**, *2*, 244.
(10) Adams, J.; Gronski, W. *Makromol. Chem., Rapid Commun.* **1989**, *10*, 553.
(11) Adams, J.; Sanger, J.; Tefehne, C.; Gronski, W. *Macromol. Chem., Rapid Comm.* **1994**, *15*, 879.
(12) Bohnert, P.; Finkelmann, H. *Macromol. Chem. Phys.* **1994**, *195*, 685.
(13) Angeloni, A. S.; Bignozzi, M. C.; Laus, M.; Chiellini, E.; Galli, G. *Polym. Bull.* **1993**, *31*, 387.
(14) Perly, B.; Douy, A.; Gallot, B. *Makromol. Chem.* **1976**, *177*, 2569.
(15) Nakajima, A.; Hayashi, T.; Kugo, K.; Shinoda, K. *Macromolecules* **1979**, *12*, 840.
(16) Barenberg, S.; Anderson, J. M.; Geil, P. H. *Int. J. Biol. Macromol.* **1981**, *3*, 382.
(17) Douy, A.; Gallot, B. *Polymer* **1987**, *28*, 147.
(18) Baker, G. L.; Bates, F. S. *Macromolecules* **1984**, *17*, 2619.
(19) Chien, J. C. W.; Wnek, G. E.; Karasz, F. E.; Hirsch, J. A. *Macromolecules* **1981**, *14*, 479.
(20) Enkelman, V.; Muller, W.; Wegner, G. *Synth. Met.* **1979/1980**, *1*, 185.
(21) Stowell, J. A.; Amass, A. J.; Beevers, M. S.; Farren, T. R. *Polymer* **1989**, *30*, 195.
(22) Saunders, R. S.; Cohen, R. E.; Schrock, R. R. *Macromolecules* **1991**, *24*, 5599.
(23) (a) Chen, J.; Thomas, E.; Ober, C.; Hwang, S.; Mao, G. *APS Bull.* **1994**, *39*, 695. (b) Chen, J. T.; Thomas, E. L.; Ober, C. K.; Hwang, S. S. *Macromolecules* **1995**, *28*, 1688.
(24) Radzilowski, L. H.; Wu, J. L.; Stupp, S. I. *Macromolecules* **1993**, *26*, 879.
(25) Radzilowski, L. H.; Stupp, S. I. *Macromolecules* **1994**, *27*, 7747.
(26) Skoulios, A. E. *Acta Crystallogr.* **1961**, *14*, 419.
(27) Herman, G. T. *Image Reconstruction from Projections*; Academic Press: New York, 1980.
(28) Hoppe, W.; Hegerl, R. In *Computer Processing of Electron Microscope Images*; Hawkes, P. W., Ed.; Springer-Verlag: Berlin, 1980.
(29) Frank, J.; Radermacher, M. In *Advanced Techniques in Biological Electron Microscopy*; Koehler, J., Ed.; Springer-Verlag: Berlin, 1986.
(30) Rosenfeld, A.; Kak, A. C. *Digital Picture Processing*, 2nd ed.; Academic Press: New York, 1982; Vol. 1.
(31) Frank, J., Ed. *Electron Tomography: Three Dimensional Imaging with the Transmission Electron Microscope*; Plenum: New York, 1992.
(32) Mellena, J. E. In *Computer Processing of Electron Microscope Images*; Hawkes, P. W., Ed.; Springer-Verlag: Berlin, 1980.
(33) Dover, S. D.; Elliot, A.; Kernaghan, A. K. *J. Microsc. (Oxford)* **1982**, *122*, 23.
(34) Olins, D. E.; Olins, A. L.; Levy, H. A.; Durfee, R. C.; Margle, S. M.; Tinnel, E. P.; Dover, S. D. *Science* **1983**, *220*, 498.
(35) Ellisman, M. H.; Lindsey, J. D.; Carragher, B. O.; Kiyonaga, S. H.; McEwen, L. R.; McEwen, B. F. 30th Annual Meeting of the American Society for Cell Biology, San Diego, CA, 1990 (abstracted in *J. Cell Biol.*, **1990**, *5, part 2*, 199A).
(36) Spontak, R. J.; Williams, M. C.; Agard, D. A. *Polymer* **1988**, *29*, 387.
(37) Spontak, R. J.; Smith, S. D.; Agard, D. A. 35th IUPAC International Symposium on Macromolecules, 1994.
(38) Spontak, R. J.; Fung, J. C.; Braunfeld, M. B.; Sedat, J. W.; Agard, D. A.; Kane, L.; Smith, S. D.; Satkowski, M. M.; Ashraf, A.; Hajduk, D. A.; and Gruner, S. M.; *Macromolecules* **1996**, *29*, 4494.
(39) Carvahlo, B. L.; Thomas, E. L. *Phys. Rev. Lett.* **1994**, *73*, 3321.
(40) Turner, M. S.; Maaloum, M.; Ausserre, D.; Joanny, J.-F.; Kunz, M. *J. Phys. II* **1994**, *4*, 689.
(41) Liu, Y.; Rafailovich, M. H.; Sokolov, J.; Schwarz, S. A.; Bahal, S. *Macromolecules* **1996**, *29*, 899.
(42) Liu, Y.; et al. *Macromolecules* **1994**, *27*, 4000.
(43) Henkee, C. S.; Thomas, E. L.; Fetters, L. J. *J. Mater. Sci.* **1988**, *23*, 1685.
(44) Semenov, A. N. *Sov. Phys. JETP* **1985**, *61*, 733.
(45) Oldmstead, P. D.; Milner, S. T. *Phys. Rev. Lett.* **1994**, *72*, 936.
(46) Gido, S. P.; Schwark, D. W.; Thomas, E. L.; Goncalves, M. *Macromolecules* **1993**, *26*, 2636.
(47) Milner, S. T. *J. Polym. Sci., Part B: Polym. Phys.* **1994**, *32*, 2743.
(48) Mansky, P.; Chaikin, P.; Thomas, E. L. *J. Mater. Sci.* **1995**, *30*, 1987.
(49) Thomas, E. L.; Kinning, D. J.; Alward, D. B.; Henkee, C. S. *Macromolecules* **1987**, *20*, 2934.
(50) Semenov, A. N. *Macromolecules* **1989**, *22*, 2849.
(51) Frank, J., Ed. *Electron Tomography*; Plenum Press: New York, 1992.
(52) Radermacher, M. Weighted back-projection methods. In *Electron Tomography*; Frank, J., Ed.; Plenum Press: New York, 1992.
(53) Crowther, R. A.; DeRosier, D. J.; Klug, A. *Proc. R. Soc. London A* **1970**, *317*, 319.
(54) Soto, G. E.; Young, S. J.; Martone, M. E.; Deerinck, T. J.; Lamont, S. P.; Carragher, B. O.; Hama, K.; Ellisman, M. H. *NeuroImage* **1994**, *1*, 230.

MA9609700